This is the accepted manuscript made available via CHORUS. The article has been published as:

Surface Phonon Polariton-Mediated Near-Field Radiative Heat Transfer at Cryogenic Temperatures

Shen Yan, Yuxuan Luan, Ju Won Lim, Rohith Mittapally, Amin Reihani, Zhongyong Wang, Yoichiro Tsurimaki, Shanhui Fan, Pramod Reddy, and Edgar Meyhofer

Phys. Rev. Lett. **131**, 196302 — Published 9 November 2023

DOI: 10.1103/PhysRevLett.131.196302

Surface phonon polariton-mediated near-field radiative heat transfer at cryogenic temperatures

Shen Yan,[1,*] Yuxuan Luan,[1,*] Ju Won Lim,[2] Rohith Mittapally,[1] Amin Reihani,[1] Zhongyong Wang,[1] Yoichiro Tsurimaki[3], Shanhui Fan[3,#], Pramod Reddy,[1,|] and Edgar Meyhofer[1,§]

[1]*Department of Mechanical Engineering, University of Michigan, Ann Arbor, MI 48109, USA*

[2]*Department of Materials Science, University of Michigan, Ann Arbor, Michigan 48109, USA*

[3]*Department of Electrical Engineering, Stanford University, USA*

ABSTRACT. Recent experiments, at room temperature, have shown that near-field radiative heat transfer (NFRHT) via surface phonon polaritons (SPhPs) exceeds the blackbody limit by several orders of magnitude. Yet, SPhP-mediated NFRHT at cryogenic temperatures remains experimentally unexplored. Here, we probe thermal transport in nanoscale gaps between a silica sphere and a planar silica surface from 77 K – 300 K. These experiments reveal that cryogenic NFRHT has strong contributions from SPhPs and does not follow the T^3 temperature (T) dependence of far-field thermal radiation. Our modeling based on fluctuational electrodynamics shows that the temperature-dependence of NFRHT can be related to the confinement of heat transfer to two narrow frequency ranges and is well accounted for by a simple analytical model. These advances enable detailed NFRHT studies at cryogenic temperatures that are relevant to thermal management and solid-state cooling applications.

Near-field radiative heat transfer (NFRHT) arises between a hot emitter (at temperature $T + \Delta T$) and a cold receiver (at temperature T) when they are separated by gaps much smaller than the Wien's wavelength (λ_w, where $\lambda_w \cdot T = 2890$ μm·K) and is of great current interest due to the novel heat transfer phenomena that arise at the nanoscale [1-4]. NFRHT is also critical to thermophotovoltaics [5-10], photonic refrigeration [11,12] and thermal management [13,14]. A key breakthrough in the field [15-19] has been the demonstration that NFRHT rates at room temperature (λ_w is ~10 μm) exceed the blackbody limit by many orders of magnitude due to strong contributions by surface phonon polaritons (SPhPs) that are supported by dielectric materials like silica (SiO_2) [20].

Despite the strong potential of SPhPs for tuning and controlling NFRHT, all SPhP-dominated NFRHT studies, leveraging a variety of geometries [1,21,22] (sphere-plane, tip-plane and plane-plane), have been limited to room and elevated temperatures due to experimental challenges in performing NFRHT measurements at nanoscale gaps and cryogenic temperatures. These limitations have prevented exploration and control of NFRHT via the use of superconductors [23-25], magnetic fields [26,27], and topological materials [28,29] that require measurements at cryogenic temperatures. Further, knowledge of NFRHT at cryogenic temperatures is essential to understand the limits to solid-state refrigeration [30] at low temperatures where parasitic heat transfer due to NFRHT from thin films of silica can become a limiting factor.

While Wien's wavelength increases with decreasing temperature, suggesting that near-field phenomena become experimentally readily accessible at cryogenic temperature, the near-field radiative heat flux decreases significantly, making NFRHT measurements at low temperature extremely challenging as higher calorimetric resolution is required. In fact, past attempts [31-37]

to study NFRHT phenomena at low temperatures employed macroscopic (millimeter to centimeter scale) devices to achieve measurable heat fluxes. However, this limited the minimum achievable gap sizes to be ~1 μm, making it impossible to probe truly nanoscale effects. Therefore, to date, systematic NFRHT experiments at cryogenic temperatures (i.e., probing NFRHT with both emitting and absorbing materials at cryogenic temperatures) and nanoscale gaps has not been possible.

To overcome this challenge and systematically characterize the temperature-dependence of NFRHT phenomena at cryogenic temperatures, we implemented a novel experimental platform. Our approach, shown schematically in Fig. 1, employs an emitter device featuring a planar surface and a spherical receiver. Briefly, the microfabricated emitter device (Fig. 1c, see SM for details of fabrication), made from silicon (Si), features a suspended region with an integrated mesa that is coated with a 2 μm-thick silica (SiO_2) layer. Further, the emitter features an integrated platinum (Pt) serpentine line that can be used to modulate the temperature of the emitter via Joule heating. The microfabricated receiver device (Fig. 1b), with T-shaped beams to reduce possible deflections, is made of silicon nitride (SiN) and features a Pt line that is used as a thermometer (see SM for details of fabrication). Further, a smooth 70 μm-diameter SiO_2 sphere (roughness quantified in SM) is integrated into the receiver via a custom process (see SM) developed by us. In order to measure the gap (d) dependent NFRHT between the emitter and the receiver, we place the spherical surface of the receiver in close proximity to the surface of the temperature-controlled emitter using a scanning probe instrument (Createc LT-SPM). Next, we modulate the temperature of the emitter at a suitably chosen frequency, while simultaneously measuring modulations in the receiver temperature arising due to the heat flux from the emitter to the receiver (the temperature modulation causes negligible levels of deflections in the emitter, see SM). As can be seen from the

resistance network shown in Fig. 2b, knowledge of the amplitude of temperature oscillations of the receiver and the emitter, along with the temperature-dependent thermal resistances, enables us to quantify the gap-dependent near-field thermal conductance at any given temperature in the 77 – 300 K range.

In order to illustrate our approach, we present in Fig. 2 data from representative experiments performed at 100 K. In these experiments, the spherical surface of the receiver was placed in close proximity (~80 nm) to the planar surface of the emitter (see Fig. 1a) such that the bottom of the sphere is directly above the center of the emitter. The emitter temperature was then modulated by an amplitude of $\Delta T_{\text{emitter}}$ = 3 K at a frequency ($2f$ = 2 Hz), by supplying an AC current with amplitude 2 mA and frequency f = 1 Hz. Simultaneously, the temperature change of the receiver ($\Delta T_{\text{receiver}}$) was measured by supplying a DC current ($I_{\text{DC,sensing}}$) of 10 μA through the receiver's Pt thermometer (see SM for details).

The data in the top panel of Fig. 2a show how the emitter-receiver gap size is systematically reduced in steps of ~0.8 nm via a piezoelectric actuator, whereas the bottom panel shows the measured amplitude of the temperature oscillations of the receiver device ($\Delta T_{\text{receiver}}$) in a bandwidth of 16 mHz. The sudden jump (marked in red in Fig 2a) corresponds to the point at which the receiver and the emitter make physical contact [3]. The minimum achievable gap size before contact in these experiments is limited by the surface roughness and stiffness of the emitter and the receiver and was estimated to be ~20 nm in our experiments (see SM for details).

In Fig. 2c we show (blue circles) the measured near-field thermal conductance (G_{NFRHT}), which is obtained from the ($\Delta T_{\text{receiver}}$) data shown in Fig. 2a by using the expression $G_{\text{NFRHT}}(T) = G_{\text{receiver}}(T) \times \Delta T_{\text{receiver}} / (\Delta T_{\text{emitter}} - \Delta T_{\text{receiver}})$, where T is the temperature at which the measurements are made. The thermal conductance of the receiver G_{receiver} is ~0.84 μW/K at 100 K for a frequency

of 2 Hz (see SM for details). It can be seen that the data (blue circles) span a relatively small range of gap sizes from 20 nm – 120 nm, because the range of motion of the piezoelectric actuator is reduced to somewhat small values at low temperatures (see SM for determination of piezo constants at different temperatures). We increased the range of gap sizes to 180 nm by adopting an approach to concatenate coarse stepping and fine, continuous piezo motions (Fig. 2c, see SM for detail). We did not further increase the range of our measurements, as G_{NFRHT} is less dependent on gap size above ~180 nm. We note that the 2 μm-thick SiO_2 films effectively acts like a semi-infinite SiO_2 layer as the gap sizes in our experiments are much smaller than the film thickness, hence there is no effect of the underlying Si substrate on our measurement. The expectation that for small gap sizes a 2 μm-thick SiO_2 film behaves effectively like a bulk SiO_2 substrate is also confirmed by detailed calculations shown in the SM.

Next, we investigated the temperature dependence of NFRHT by performing similar measurements at four other temperatures (77 K, 150 K, 220 K and 300 K) using the same emitter and receiver devices described above. To implement these measurements, we first characterized the thermal conductance and the frequency response of the receiver and the emitter device at each temperature (see SM for details of the thermal characterization of the emitter and receiver based on the 3ω method [38]). Subsequently, we performed measurements of the gap size-dependent NFRHT as described above and used these data, along with the measured temperature-dependent thermal conductance of the receiver, $G_{\mathrm{receiver}}(T)$, to obtain the temperature-dependent near-field conductance $G_{\mathrm{NFRHT}}(T)$ as described above. The measured gap size-dependent radiative thermal conductance at each temperature is shown in Fig. 3a. From these data it can be seen that, at all temperatures, there is a significant increase (~3 – 4 folds) in the thermal conductance as the gap size is decreased from ~120 nm to 20 nm. This highlights the fact that SPhPs continue to play a

major role in heat transfer at the nanoscale even at cryogenic temperatures. The data in Fig. 3a also show that, at any given gap size, NFRHT is higher for a higher ambient temperature. To better understand the temperature dependence of NFRHT, we plot in the inset of Fig. 3a the near-field conductance as a function of temperature for various gap sizes. As can be seen, the thermal conductance drops rapidly as the temperature decreases and the observed temperature dependence is different from the T^3 dependence expected for far-field thermal radiation.

In order to understand the observed NFRHT behavior, we performed detailed calculations within the framework of fluctuational electrodynamics [39] and the scattering matrix [40] approach. Specifically, we computed (see SM for details of our model) the spectral conductance $h(\omega, T, d)$ between plane parallel surfaces of an emitter consisting of a 2 μm-thick SiO_2 film on a semi-infinite silicon substrate and a semi-infinite SiO_2 receiver separated by a 20 nm gap (see the geometry inset of Fig. 3c) using the following expression[1,3,4,21]:

$$h(\omega, T, d) = \frac{1}{4\pi^2}\frac{\partial}{\partial T}\left[\frac{\hbar\omega}{e^{\hbar\omega/k_B T}-1}\right]\int_0^\infty \tau(\omega, k)\, k dk \quad , \tag{1}$$

where ω is the angular frequency of the radiation, k is the magnitude of the wavevector component parallel to the planes, k_B is the Boltzmann constant, $\hbar$ is the reduced Planck's constant, and $\tau(\omega,k)$ is the transmission function (see SM for details of how $\tau(\omega,k)$ is evaluated). For comparison, in the inset of Fig. 3b the spectral conductance for two blackbodies in the far-field ($h_B(\omega, T, d)$) is also shown at various temperatures. In strong contrast to blackbodies in the far-field, where the spectral conductance is broadband, NFRHT for SiO_2 (gap size <100 nm) shown in Fig. 3b is dominated by SPhPs at two narrow ranges of frequencies centered around 0.06 eV and 0.14 eV. Moreover, it can be seen that, as the temperature decreases, the contribution from the higher energy

SPhPs at 0.14 eV decreases rapidly due to a steep decrease in the excitation of SPhPs, which depends on the Bose-Einstein distribution.

By integrating the spectral conductance, the temperature and gap-dependent near-field conductance ($h(T,d)$) between two parallel planes is obtained (Fig. 3c). Subsequently, we employed the Derjaguin-approximation [41] along with the data from Fig. 3c to compute the gap-dependent thermal conductance for the sphere-plane geometry employed in our experiments (specifically we calculated the near-field contributions using the Derjaguin approximation and far-field contributions by carefully quantifying the view factor for this sphere-plane geometry, see details in the SM, which includes Refs. [42-46]). The data obtained from these calculations (scaled by a factor of $(2.5)^{-1}$) are shown in Fig. 3d (inset schematically describes the Derjaguin-approximation). We note that a similar scaling factor was found to be necessary in past work at room temperature [3] for achieving good agreement between theory and experiment and was attributed to uncertainties in the microstructure (i.e., surface roughness/porosity) and dielectric properties of the materials. As can be seen in Fig. 3d, the computational results agree well with experimental data at room temperature, but show some deviation at intermediate temperatures, especially at gap sizes smaller than 30 nm, which we address below. Finally, we note that these calculations also confirm that the radiative thermal conductance is significantly reduced upon decreasing the temperature, corresponding to an approximately 100-fold reduction in the conductance at any given gap size when the temperature is lowered from 300 K to 77 K.

To understand the origin of the temperature-dependence of NFRHT, we plot the experimental data at 20 nm gap size (the smallest gap size used in our experiments) as well as the computational data for the planar devices as a function of temperature in Fig. 4a (all data normalized by the corresponding conductance at 300 K). It can be seen that the temperature-

dependence is nearly identical in both plane-plane and sphere-plane geometries, highlighting that the temperature-dependence observed in the experiments can be examined by analyzing the temperature-dependence in the plane-plane geometry. These computational results also agree well with our experimental data (see dash-dot line in the Fig. 4a) and deviate from the T^3dependence expected for far-field thermal radiation. The observed deviation from both experiments and computations indicate that the distinct temperature-dependence of NFRHT possibly originates from the SPhPs. To confirm that SPhPs are indeed the origin of the temperature-dependence of NFRHT, we first plot the dispersion relation for SPhPs (Fig. 4b, see SM for details of how the dispersion relation is obtained based on Ref. [47]), which clearly shows that SPhPs are supported over a narrow range of frequencies, which also align well with the peaks in the integrated transmission function $\tau(\omega) = \frac{1}{2\pi}\int_0^\infty \tau(\omega, k)\, k dk$ shown in Fig. 4c. Because the dominant contribution to $\tau(\omega)$ comes from the two SPhPs peaks, we describe $\tau(\omega)$ as a linear combination of two Lorentzian functions:

$$\tau(\omega) = \sum_{i=1,2} \frac{A_i \Gamma_i}{\left[\left(\omega - \omega_{0,i}\right)^2 + \Gamma_i^2\right]}, \quad (2)$$

where A_i, $\omega_{0,i}$, and Γ_i are the fitting parameters for each peak of $\tau(\omega)$. The obtained fit is shown in Fig. 4c (fitting parameters in SM) and is found to closely approximate the original $\tau(\omega)$. Using Eqs. 1, 2 and $h(T,d) = \int_0^\infty h(\omega, T, d)\, d\omega$, we recompute the near-field radiative heat conductance and plot it in Fig. 4a (red open squares), which is in good agreement with the full computations using Eq. 1. Next, we obtained an approximate analytical expression for h (T, d) following (see SM for details, which includes Refs. [48-50]):

$$h(T,d) \sim \sum_{i=1,2} \int_0^\infty \frac{d\omega}{2\pi} \frac{k_B e^{\frac{\hbar\omega}{k_B T}} \left(\frac{\hbar\omega}{k_B T}\right)^2}{\left(e^{\frac{\hbar\omega}{k_B T}} - 1\right)^2} \frac{A_i \Gamma_i}{\left(\omega - \omega_{0,i}\right)^2 + \Gamma_i^2} \sim \sum_{i=1,2} \frac{A_i \hbar^2 \omega_{0,i}^2}{2 k_B T^2} \frac{e^{\frac{\hbar\omega_{0,i}}{k_B T}}}{\left(e^{\frac{\hbar\omega_{0,i}}{k_B T}} - 1\right)^2} \quad (3)$$

The above equation suggests that each Lorentzian in $\tau(\omega)$ makes a temperature-dependent contribution of the form $\frac{1}{T^2} \frac{e^{\hbar\omega_{0,i}/k_B T}}{\left(e^{\hbar\omega_{0,i}/k_B T} - 1\right)^2}$, which does not scale as T^3. The temperature dependence of near-field radiative heat conductance predicted by this simpler analytical expression in Eq. 3 is then plotted in Fig. 4a (solid line), which shows excellent agreement with both experimental data and the results from full computations given by Eq. 1, while clearly deviating from the T^3 dependence expected for far-field thermal radiation.

Finally, we note that in all the analysis presented above we assumed that the dielectric function is independent of temperature for the range of temperatures explored in this work. This assumption can be relaxed following past work [51,52], which suggests that the effect of temperature can be captured by introducing a weakly temperature-dependent damping in the dielectric function of SiO_2 (discussed in detail in SM section 14, which also includes Ref. [53]). Upon accounting for this temperature dependence (see SM for details), the obtained gap-dependent near-field thermal conductance is presented in Fig. 4d. As can be seen, assuming a temperature-dependent dielectric function leads to some additional improvement in the agreement between experiment and theory, especially at gap sizes smaller than 30 nm. These results highlight that incorporating the temperature dependence of dielectric functions is likely necessary for improved qualitative and quantitative agreement between experiments and theory.

To summarize, we performed first systematic measurements of radiative heat transfer in nanoscale gaps between polar dielectrics at cryogenic temperatures (77 K to 300 K). We show that

the temperature dependence of NFRHT between polar dielectrics is significantly different from far-field RHT and attribute the differences to the narrow range of frequencies over which heat is transported by SPhPs in polar dielectrics. Our experimental results are found to be in good agreement with detailed calculations based on fluctuational electrodynamics. Further, we obtain a simple analytical expression for the observed temperature dependence. The experimental techniques established in this work are also expected to enable future experimental exploration of a number of currently untested theoretical and computational predictions, regarding NFRHT phenomena in superconductors, magnetic fields, and topological materials that are expected to arise at cryogenic temperatures.

ACKNOWLEDGEMENTS

E.M. and P.R. acknowledge support from DOE-BES through a grant from the Scanning Probe Microscopy Division under award No. DESC0004871 (experiments), from the Army Research Office under award No. MURI W911NF-19-1-0279 (fabrication of devices), from the Office of Naval Research under award No. N00014-20-1-2476 (instrumentation) and the National Science Foundation Grant No. 1803983 (analysis). We acknowledge the Lurie Nanofabrication Facility and the Michigan Center for Materials Characterization for facilitating the fabrication and calibration of devices.

[*]These authors contributed equally to this work.

[#]Corresponding author.

shanhui@stanford.edu

[|]Corresponding author.

pramodr@umich.edu

[§]Corresponding author.

meyhofer@umich.edu

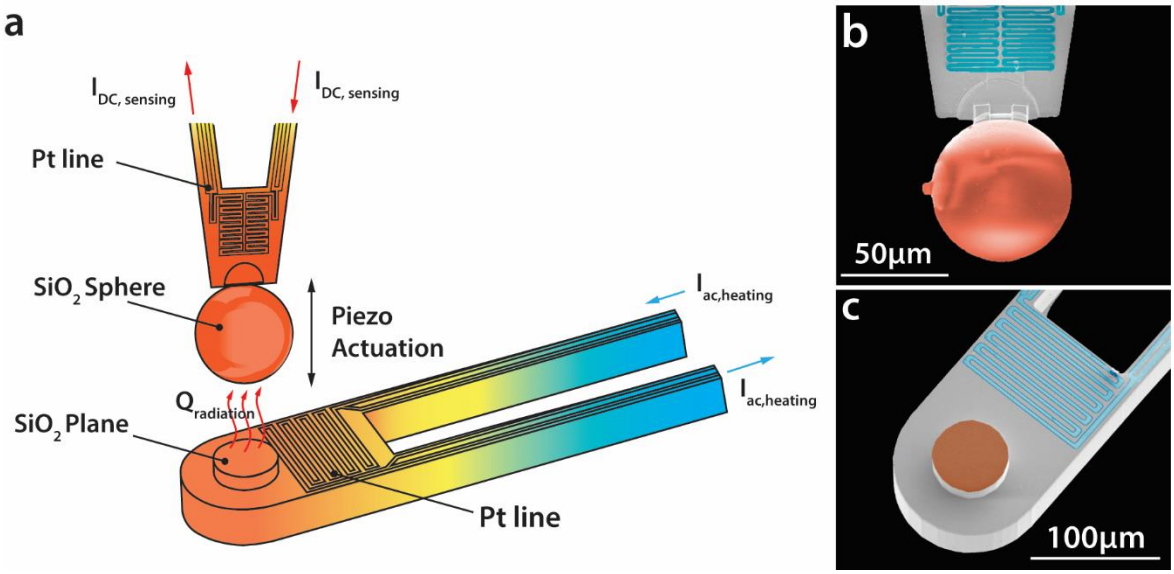


FIG. 1. Schematic of the NFRHT measurement platform integrated into a variable temperature scanning probe instrument and scanning electron microscopy (SEM) images of the employed devices. a) Emitter (bottom) and a receiver (with integrated sphere, top). The silicon-based emitter has an integrated Pt heater and a 15 µm-tall mesa that is coated with a 2 µm-thick SiO_2 layer. The receiver consists of an integrated Pt resistance sensor and a 70 µm-diameter silica sphere. The heat current ($Q_{radiation}$) is measured by modulating the emitter temperature via an AC current ($I_{ac,\ heating}$) supplied to the integrated Pt line and measuring the resulting temperature oscillations of the receiver by supplying a DC current ($I_{DC,\ sensing}$) to its Pt thermometer. The gap size between the emitter and the receiver is controlled via a piezo actuator. b) SEM image of the receiver with integrated sphere. c) SEM image of the emitter featuring a Pt sensor (blue) and the SiO_2-coated mesa (brown).

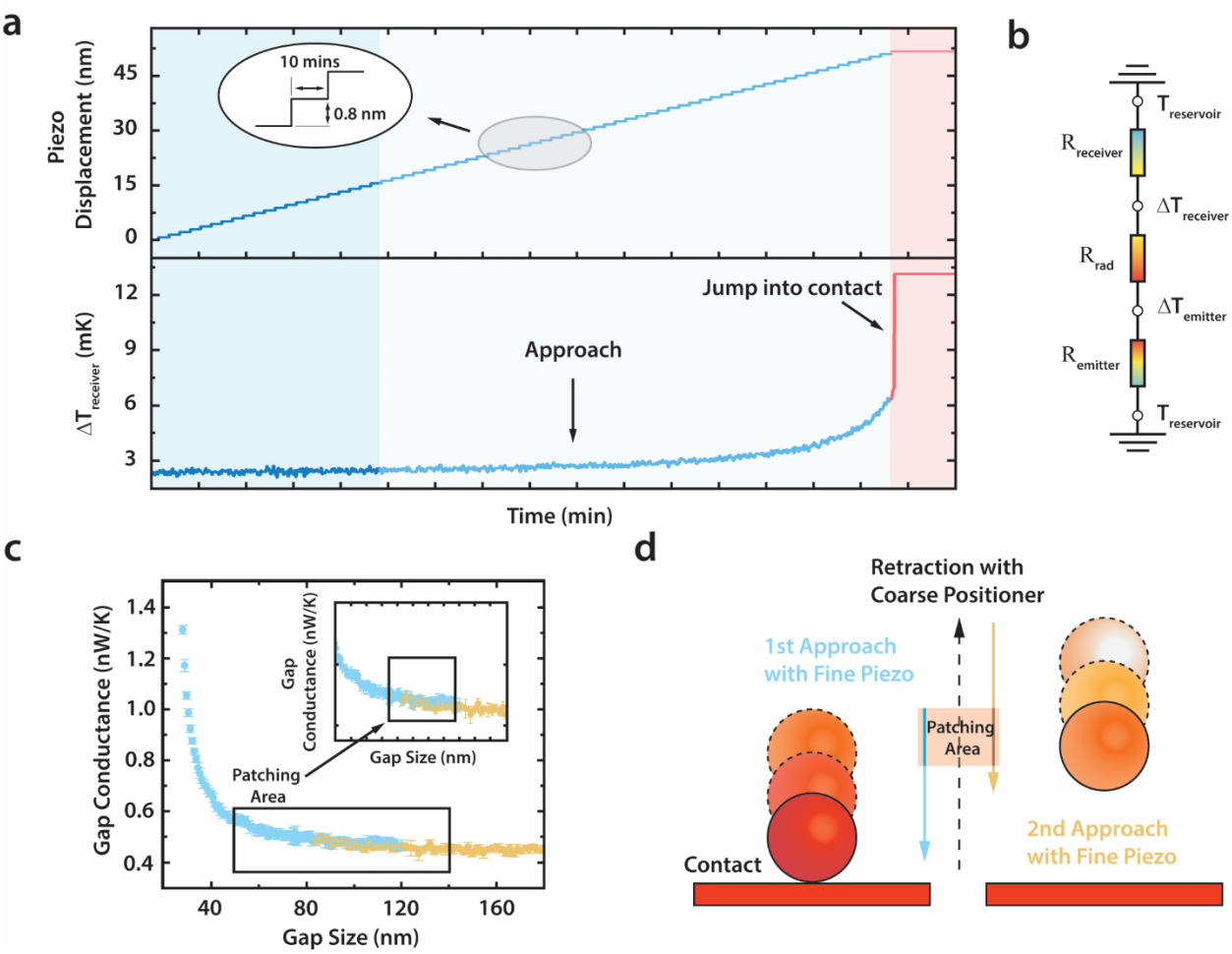


FIG. 2. Experimental approach for probing NFRHT at cryogenic temperatures. a) Data obtained in a measurement performed at 100 K. The top panel shows how the separation between the receiver and the emitter is varied, via a piezoelectric actuator, in steps of ~0.8 nm. The bottom panel depicts the measured temperature rise of the receiver as a function of gap size. Contact between the emitter and the receiver is signaled by a jump in the temperature (marked red) of the receiver. b) Thermal resistance network of the radiative heat transfer between the emitter and the receiver. c) Measured thermal conductance with error bars as a function of gap size. To increase the range, we spliced two high resolution gap conductance records. The overlapping region of the conductances (see inset) enables us to concatenate the data. d) Schematic description of the process of concatenation. The first approach contains information till contact. The second approach starts by retracting the receiver by a coarse positioner. Subsequently, the receiver device was displaced towards the emitter until heat flux signal exceeded the smallest signal measured in the first approach.

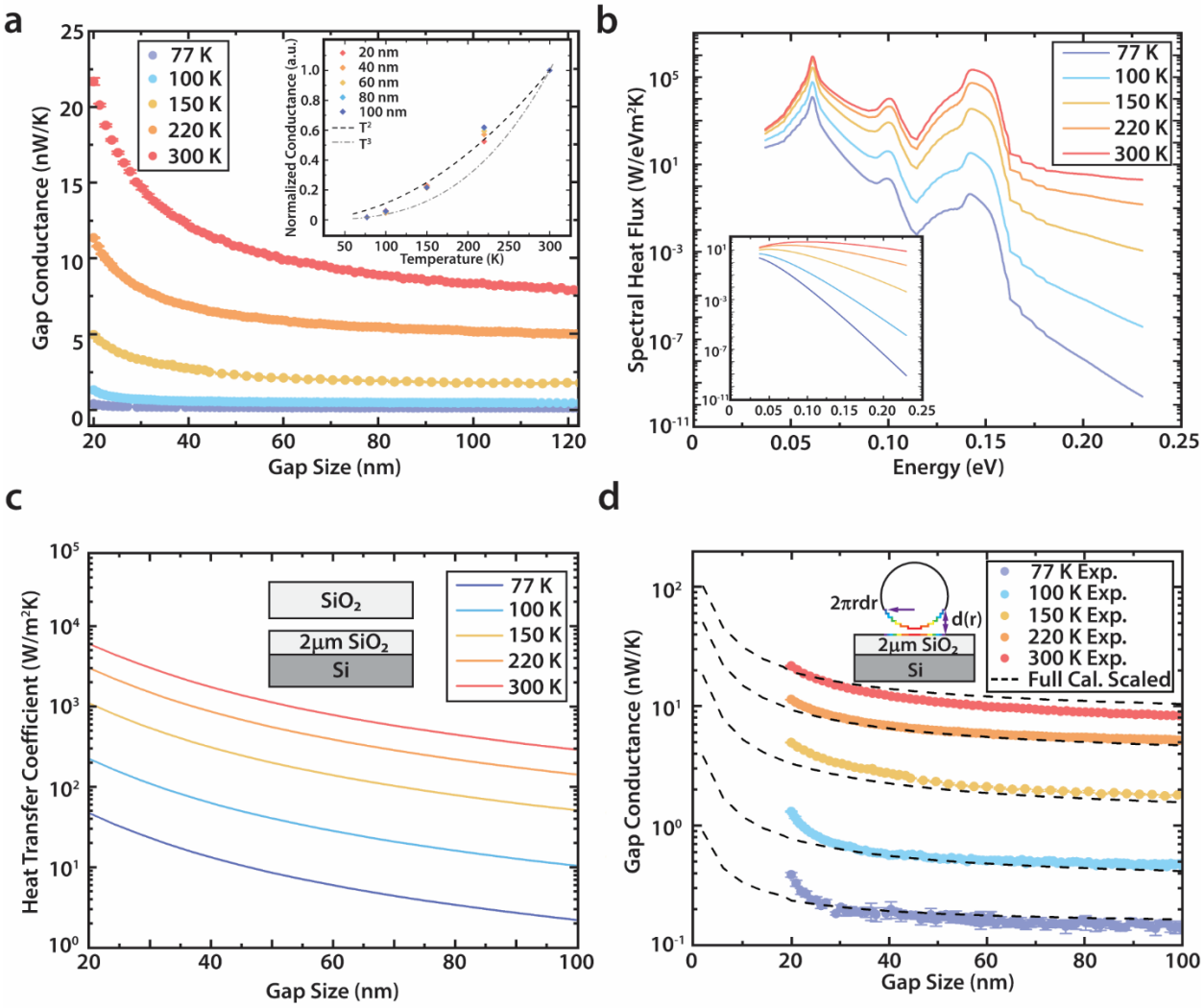


FIG. 3. Gap size and temperature dependence of near-field thermal conductance. (a) Measured near-field thermal conductance as a function of gap size at different temperatures for an emitter device coated with a 2 μm-thick layer of SiO_2 and a receiver device with a 70 μm-diameter SiO_2 sphere. The inset depicts the temperature dependence of near-field thermal conductance (normalized to the value at 300 K) at various gap sizes using the data from panel (a). The two dashed lines represent the expected conductance following T^3 and T^2 temperature dependence. (b) The spectral heat flux for silica surfaces in the near-field (geometry corresponds to that shown in the inset of Fig. 3c for a gap size of 20 nm). The spectral heat flux between two semi-infinite blackbodies in the far-field of each other is shown in the inset. (c) The computational results of the temperature-dependent NFRHT in the plane-plane geometry using fluctuational electrodynamics (inset shows the geometry that is modelled). (d) Computational results for the gap-dependent NFRHT, at various temperatures, in the sphere-plane geometry using the Derjaguin approximation (inset illustrates the Derjaguin approximation method). The computed values were scaled as described in the main text. Note that most of the error bars shown in panel (a) and (d) are smaller than the symbols.

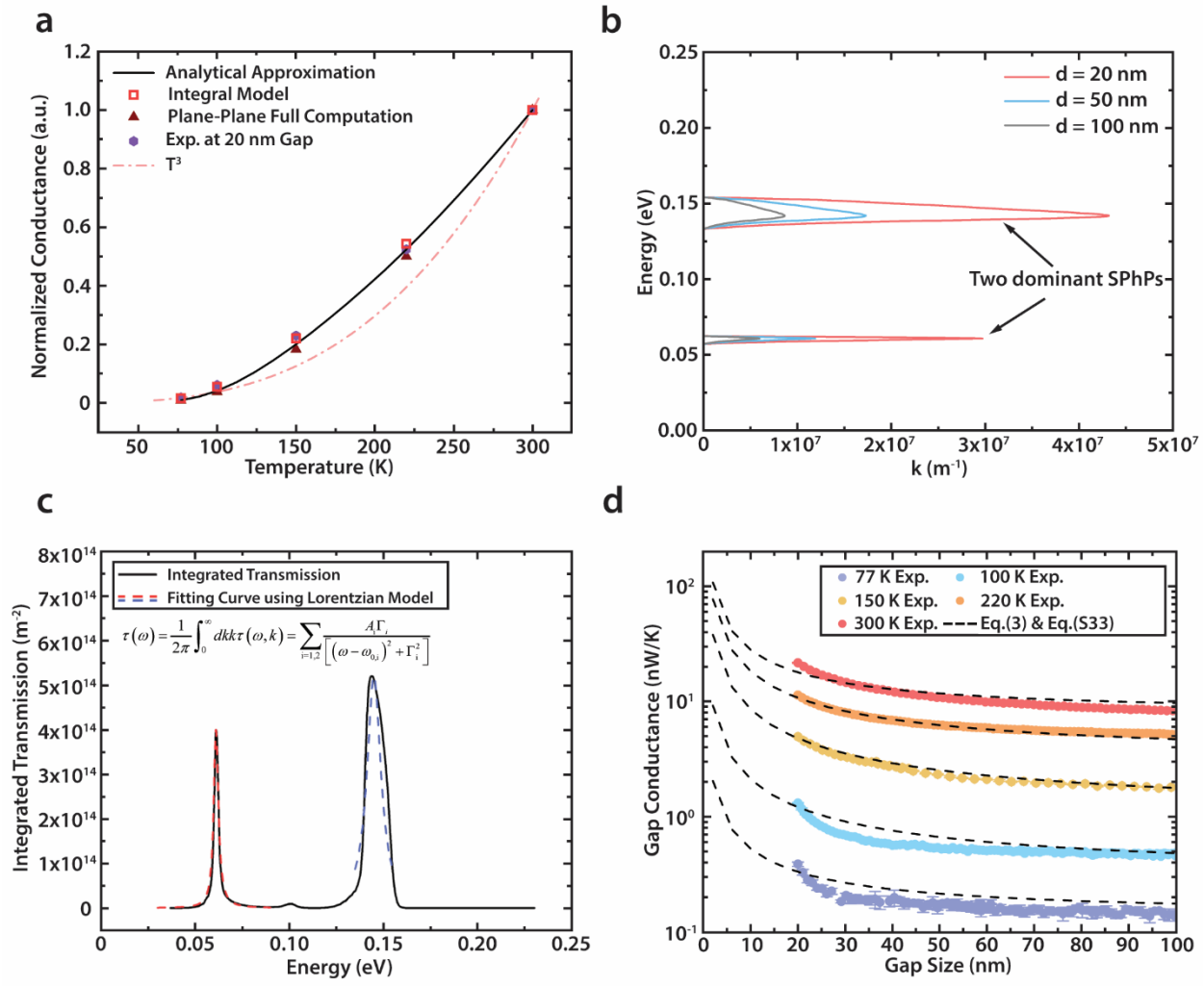


FIG. 4. Illustration of the origin of the observed temperature dependence. (a) Comparison of experimental data with various computational and analytical models. Computational results for the plane-plane structure show the same temperature dependence as experimental data but deviate from a T^3 dependence, which holds for far-field radiative heat transfer. See details of the models in SM. (b) The dispersion relation at different gap sizes between two SiO_2 planes. (c) The integrated transmission as a function of energy. The two SPhP-resonant peaks are fitted by two Lorentzian functions shown by dashed lines. (d) Fitted analytical model based on Eq. (3), which is found to be in good agreement with the experimental data (most of the error bars are smaller than the symbols). Additional details in SM.

References:

[1] S. A. Biehs, R. Messina, P. S. Venkataram, A. W. Rodriguez, J. C. Cuevas, and P. Ben-Abdallah, Rev Mod Phys **93** (2021).
[2] L. Rincón-García, D. Thompson, R. Mittapally, N. Agraït, E. Meyhofer, and P. Reddy, Physical Review Letters **129**, 145901 (2022).
[3] B. Song *et al.*, Nature nanotechnology **10**, 253 (2015).
[4] A. Volokitin and B. N. Persson, Rev Mod Phys **79**, 1291 (2007).
[5] A. Narayanaswamy and G. Chen, Applied Physics Letters **82**, 3544 (2003).
[6] M. Laroche, R. Carminati, and J.-J. Greffet, Journal of applied physics **100**, 063704 (2006).
[7] A. Fiorino, L. Zhu, D. Thompson, R. Mittapally, P. Reddy, and E. Meyhofer, Nature nanotechnology **13**, 806 (2018).
[8] B. Zhao, K. Chen, S. Buddhiraju, G. Bhatt, M. Lipson, and S. Fan, Nano Energy **41**, 344 (2017).
[9] R. Mittapally, B. Lee, L. Zhu, A. Reihani, J. W. Lim, D. Fan, S. R. Forrest, P. Reddy, and E. Meyhofer, Nat Commun **12** (2021).
[10] S. Basu, Z. M. Zhang, and C. J. Fu, Int J Energ Res **33**, 1203 (2009).
[11] L. X. Zhu, A. Fiorino, D. Thompson, R. Mittapally, E. Meyhofer, and P. Reddy, Nature **566**, 239 (2019).
[12] K. Chen, P. Santhanam, S. Sandhu, L. Zhu, and S. Fan, Physical Review B **91**, 134301 (2015).
[13] A. Fiorino *et al.*, ACS nano **12**, 5774 (2018).
[14] P. Van Zwol, L. Ranno, and J. Chevrier, Physical review letters **108**, 234301 (2012).
[15] M. Ghashami, H. Y. Geng, T. Kim, N. Iacopino, S. K. Cho, and K. Park, Physical Review Letters **120** (2018).
[16] H. Salihoglu, W. Nam, L. Traverso, M. Segovia, P. K. Venuthurumilli, W. Liu, Y. Wei, W. J. Li, and X. F. Xu, Nano Lett **20**, 6091 (2020).
[17] B. Song, D. Thompson, A. Fiorino, Y. Ganjeh, P. Reddy, and E. Meyhofer, Nature Nanotechnology **11**, 509 (2016).
[18] E. Rousseau, A. Siria, G. Jourdan, S. Volz, F. Comin, J. Chevrier, and J. J. Greffet, Nat Photonics **3**, 514 (2009).
[19] S. Shen, A. Narayanaswamy, and G. Chen, Nano Lett **9**, 2909 (2009).
[20] Z. M. Zhang, *Nano/microscale heat transfer* (McGraw-Hill, New York, NY, 2007).
[21] J. C. Cuevas and F. J. García-Vidal, Acs Photonics **5**, 3896 (2018).
[22] K. Kim *et al.*, Nature **528**, 387 (2015).
[23] S. G. Castillo-Lopez, G. Pirruccio, C. Villarreal, and R. Esquivel-Sirvent, Sci Rep-Uk **10** (2020).
[24] E. Moncada-Villa and J. C. Cuevas, Phys Rev Appl **15** (2021).
[25] J. Ordonez-Miranda, K. Joulain, D. D. Meneses, Y. Ezzahri, and E. Drevillon, Journal of Applied Physics **122** (2017).
[26] E. Moncada-Villa, V. Fernández-Hurtado, F. J. Garcia-Vidal, A. García-Martín, and J. C. Cuevas, Physical Review B **92**, 125418 (2015).
[27] B. Zhang, J. L. Song, L. Lu, B. W. Li, K. Zhou, Q. Cheng, and Z. X. Luo, Applied Physics Letters **117** (2020).
[28] C. Guo, B. Zhao, D. H. Huang, and S. H. Fan, Acs Photonics **7**, 3257 (2020).
[29] G. M. Tang, J. Chen, and L. Zhang, Acs Photonics **8**, 443 (2021).

[30] E. Mykkanen, J. S. Lehtinen, L. Gronberg, A. Shchepetov, A. V. Timofeev, D. Gunnarsson, A. Kemppinen, A. J. Manninen, and M. Prunnila, Sci Adv **6** (2020).
[31] G. Domoto, R. Boehm, and C. L. Tien, (1970).
[32] T. Králík, P. Hanzelka, V. Musilová, A. Srnka, and P. Urban, Cryogenics **113**, 103156 (2021).
[33] T. Kralik, P. Hanzelka, V. Musilova, A. Srnka, and M. Zobac, Review of Scientific Instruments **82**, 055106 (2011).
[34] T. Kralik, P. Hanzelka, M. Zobac, V. Musilova, T. Fort, and M. Horak, Physical review letters **109**, 224302 (2012).
[35] T. Králík, V. Musilová, T. Fořt, and A. Srnka, Physical Review B **95**, 060503 (2017).
[36] V. Musilová, T. Králík, T. Fořt, and M. Macek, Physical Review B **99**, 024511 (2019).
[37] U. F. Wischnath, J. Welker, M. Munzel, and A. Kittel, Review of scientific instruments **79**, 073708 (2008).
[38] D. G. Cahill, Review of scientific instruments **61**, 802 (1990).
[39] S. M. Rytov, I. U. r. A. Kravt͡sov, and V. i. a. n. I. i. Tatarskiĭ, *Principles of Statistical Radiophysics: Elements of Random Process Theory* (Springer, 1987).
[40] D. Whittaker and I. Culshaw, Physical Review B **60**, 2610 (1999).
[41] B. Derjaguin, I. Abrikosova, and E. Lifshitz, Quarterly Reviews, Chemical Society **10**, 295 (1956).
[42] R. Kitamura, L. Pilon, and M. Jonasz, Applied optics **46**, 8118 (2007).
[43] M. F. Modest, *Radiative heat transfer* (Academic press, 2013).
[44] M. H. N. Naraghi and B. T. F. Chung, Journal of Heat Transfer **104**, 426 (1982).
[45] A. Narayanaswamy and G. Chen, Physical Review B **77**, 075125 (2008).
[46] E. D. Palik, *Handbook of optical constants of solids* (Academic press, 1998), Vol. 3.
[47] A. Archambault, T. V. Teperik, F. Marquier, and J.-J. Greffet, Physical Review B **79**, 195414 (2009).
[48] P. Ben-Abdallah and K. Joulain, Physical Review B **82**, 121419 (2010).
[49] H. Iizuka and S. Fan, Physical Review B **92**, 144307 (2015).
[50] E. Rousseau, M. Laroche, and J.-J. Greffet, Journal of Applied Physics **111**, 014311 (2012).
[51] S. Anand, P. Verma, K. Jain, and S. Abbi, Physica B: Condensed Matter **226**, 331 (1996).
[52] X. Yang, T. Feng, J. S. Kang, Y. Hu, J. Li, and X. Ruan, Physical Review B **101**, 161202 (2020).
[53] F. Gervais and B. Piriou, Physical Review B **11**, 3944 (1975).